












# Non-reciprocal band structures in an exciton–polariton Floquet optical lattice

Received: 23 May 2023

Accepted: 20 March 2024

Published online: 23 April 2024

 Check for updates

Yago del Valle Inclan Redondo <sup>1,2</sup>✉, Xingran Xu <sup>3,4</sup>, Timothy C. H. Liew <sup>3</sup>, Elena A. Ostrovskaya <sup>5</sup>, Alexander Stegmaier <sup>6</sup>, Ronny Thomale <sup>6</sup>, Christian Schneider <sup>7</sup>, Siddhartha Dam <sup>8</sup>, Sebastian Klemmt <sup>8</sup>, Sven Höfling <sup>8</sup>, Seigo Tarucha<sup>1</sup> & Michael D. Fraser <sup>1,2</sup>✉

Periodic temporal modulation of Hamiltonians can induce geometrical and topological phenomena in the dynamics of quantum states. Using the interference between two lasers, we demonstrate an off-resonant optical lattice for a polariton condensate with controllable potential depths and nearest-neighbour coupling strength. Temporal modulation is introduced via a gigahertz frequency detuning between pump lasers, creating a polariton ‘conveyor belt’. The breaking of time-reversal symmetry causes band structures to become non-reciprocal and acquire a universal tilt given by Planck’s constant and the frequency of modulation ( $\hbar\Delta f$ ). The non-reciprocal tilting is connected to the non-trivial topology of the Floquet–Bloch bands, which have a finite Chern number. Detailed characterization of the lattice potential depth and its dynamics highlights the role of high-energy carriers in the formation of optical potential landscapes for polaritons, demonstrating the possibility of modulation faster than the polariton lifetime and opening a pathway towards Floquet engineering in polariton condensates.

The adiabatic modulation of a quantum Hamiltonian around a closed loop in parameter space causes eigenstates to acquire a geometric phase—the Berry phase<sup>1</sup>. For periodically driven systems, the additional accumulation of geometric phase can lead to the formation of novel topological invariants<sup>2</sup> and induce topologically protected transport and edge modes<sup>3–6</sup>. Combined with a spatially periodic potential, eigenstates can be defined on a Floquet–Brillouin zone<sup>7,8</sup>, and topological winding around this zone can cause non-reciprocal transport and has been observed in a wide range of spatio-temporally modulated physical systems, both classical and quantum<sup>9–13</sup>. Non-reciprocity also emerges in the shearing and tilting of the momentum-space band structure,

which is proportional to the Chern number of the Floquet–Bloch bands<sup>13–16</sup>. In this Article, the formation of non-reciprocal topological band structures is demonstrated in an exciton–polariton condensate.

Exciton–polaritons are mixed light–matter quasiparticles that emerge from the strong coupling of semiconductor microcavity photons and quantum well excitons<sup>17</sup>. Under strong non-resonant pumping, there is a phase transition from a thermal state to a quantum state with long-range spatial and temporal coherence—a polariton condensate<sup>18</sup>. Lithographic methods for engineering the polariton potential landscape have been commonly exploited to emulate the physics of many-body two-dimensional systems using polariton condensates<sup>19–22</sup>.

<sup>1</sup>RIKEN Center for Emergent Matter Science, Wako-shi, Japan. <sup>2</sup>Physics and Informatics Laboratories, NTT Research, Sunnyvale, CA, USA. <sup>3</sup>Division of Physics and Applied Physics, School of Physical and Mathematical Sciences, Nanyang Technological University, Singapore, Singapore. <sup>4</sup>School of Science, Jiangnan University, Wuxi, China. <sup>5</sup>ARC Centre of Excellence in Future Low-Energy Electronics Technologies and Department of Quantum Science and Technology, Research School of Physics, The Australian National University, Canberra, Australian Capital Territory, Australia. <sup>6</sup>Institut für Theoretische Physik und Astrophysik, Universität Würzburg, Würzburg, Germany. <sup>7</sup>Institute of Physics, University of Oldenburg, Oldenburg, Germany. <sup>8</sup>Julius-Maximilians-Universität Würzburg, Physikalisches Institut und Würzburg-Dresden Cluster of Excellence ct.qmat, Lehrstuhl für Technische Physik, Am Hubland, Würzburg, Germany. ✉e-mail: [yago.valle@a.riken.jp](mailto:yago.valle@a.riken.jp); [michael.fraser@riken.jp](mailto:michael.fraser@riken.jp)

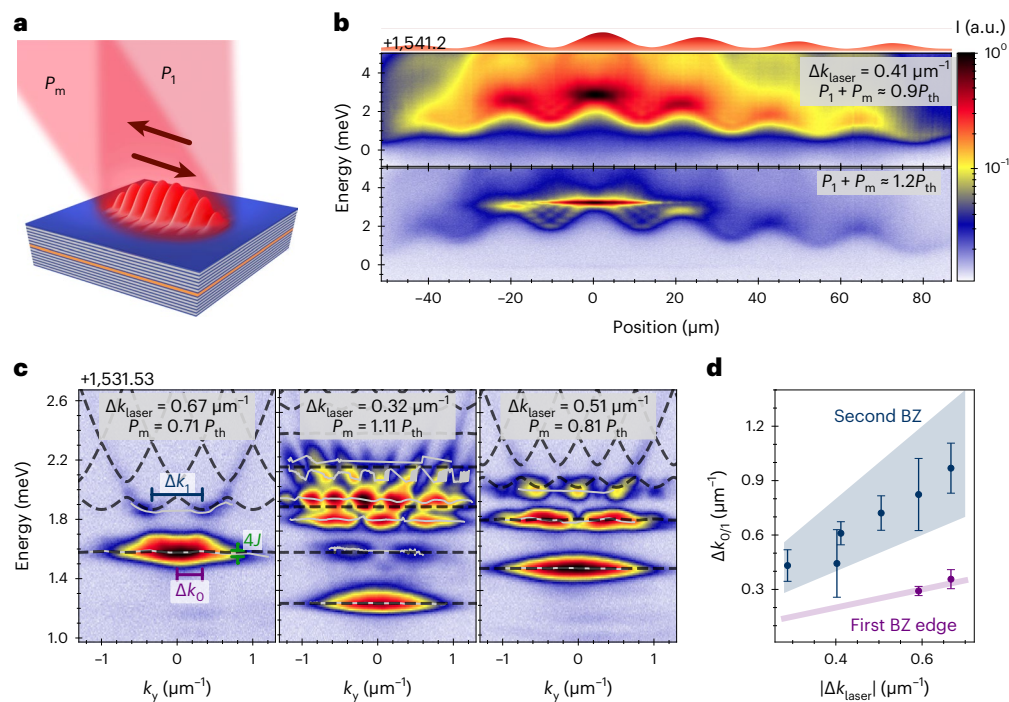


**Fig. 1 | Band structures of a polariton conveyor belt.** **a**, A diagram of the sample excitation. The angle between the lasers ( $\Delta k_{\text{laser}} = 0.3\text{--}0.7\ \mu\text{m}^{-1}$ ) controls the fringe periodicity, while the frequency offset ( $|\Delta f| < 7\ \text{GHz}$ ) controls their speed and movement. The normal-incidence laser has  $P_l = 1.2P_{\text{th}}$  with a condensation threshold  $P_{\text{th}}$  of 100 mW. The angle-offset laser has  $P_m = 1\text{--}110\ \text{mW}$ . **b**, Example real-space tomography (intensity normalized) just below and just above the condensation threshold. The red-coloured diagram on top corresponds to the intensity of the laser interference pattern. **c**, Example band structures (intensity normalized) at zero frequency offset for different lattice periods and depths. Thin white lines

show the results of spectral peak finding and clustering as described in Methods. Black dashed lines correspond to the fitted Bloch modes. The energy width of the ground state (in terms of nearest neighbour hopping  $J$ ) is marked in green. **d**, The average size of the first ( $\Delta k_0$ ) and second ( $\Delta k_1$ ) BZs as functions of  $\Delta k_{\text{laser}}$  (between 7 and 52 samples). Shaded regions correspond to the expected edge of the first BZ (purple-magenta,  $\Delta k_0 \approx \pi/a$ , where  $a$  is the fringe period) and of the boundaries of the second BZ in the extended scheme (blue-grey,  $2\pi/a < \Delta k_1 < 4\pi/a$ ). Error bars are estimated by averaging datasets with different  $P_m$ .

While there have been proposals on how to achieve non-reciprocity with such static potentials<sup>23–25</sup>, experimental demonstrations have so far been absent. An alternative to lithographic approaches for creating static potentials uses spatially patterned non-resonant optical fields. Drawing from the unique light–matter properties of polaritons, a carrier distribution proportional to the optical field interacts nonlinearly with the condensate. The created potential has both real<sup>26</sup> and imaginary (non-Hermitian)<sup>27</sup> components that have been used to create optical traps<sup>28,29</sup>, to control the hopping between individual sites<sup>30–32</sup> and to create non-Hermitian lattices<sup>33,34</sup>.

While optical fields are typically patterned via spatial phase or intensity modulation of laser wavefronts, this work uses the angled interference between two lasers to create a spatio-temporally periodic laser intensity pattern—an optical conveyor belt (Fig. 1a). We experimentally demonstrate the formation of Floquet–Bloch bands and connect the emergence of non-reciprocity in a moving conveyor belt to the Berry phase acquired through the temporal modulation and the corresponding Chern number. We additionally quantify the limit on the speed at which optical potentials can be used to modulate polariton condensates, for example, to create Floquet topological lattices<sup>35</sup>, to rotate polariton condensates<sup>36,37</sup> or to control recently proposed polariton qubits<sup>38</sup>.

## Results

Using one laser to create the interference pattern, the spatially periodic carrier distribution can be directly resolved in real space (Fig. 1b). Below threshold (top panel), the polariton ground state has a periodically modulated energy, with the highest energy at the interference maxima. Above threshold (bottom panel), there is strong emission from the

positions of maximum gain and a decrease in the background occupation, allowing us to resolve the quantized, trapped states occurring at the intensity minima where the potential energy is minimum. To achieve frequency modulation, two different lasers were used, which washes out the spatial structure over experimental imaging time scales, even for  $\Delta f \approx 0$  (Supplementary Section II). However, the polariton emission in momentum space still shows the formation of quantized states (Fig. 1c). While the exact band in which a condensate(s) forms will depend on the periodicity of the lattice<sup>29,39</sup> and the stability of the interference pattern, the band formation itself is robust and can be controlled through the angle between the lasers ( $\Delta k_{\text{laser}}$ ) and the relative power of the angled beam ( $P_m$ ). Shallow (small  $P_m$ ) and wide (small  $\Delta k_{\text{laser}}$ ) fringes lead to more closely separated bands, and vice versa (Fig. 1c), intuitively corresponding to a potential proportional to the fringe pattern. A quantitative demonstration that the periodicity of the laser interference is transferred to the polariton wavefunction is given by the formation of Brillouin zones (BZs) in the dispersion images. The distance between emission peaks of the first excited state ( $p$  band) falls within the expected second BZ in the extended scheme (Fig. 1d, blue-grey), and the distance between energy maxima of the ground state ( $s$  band) corresponds to the expected edge of the first BZ of a lattice with period  $a$  of  $2\pi/\Delta k_{\text{laser}}$  (Fig. 1d, purple-magenta). The presence of ground-state curvature additionally proves that hopping between adjacent sites is non-negligible and that interfering laser beams can provide a simpler alternative to typical wavefront shaping for the simulation of spatially periodic Hamiltonians in microcavities<sup>40</sup>.

The measured energy mode structure was compared with an excitation–photon mean-field model, where gain and polariton nonlinearity are neglected for simplicity and where the nonlinear interactions with

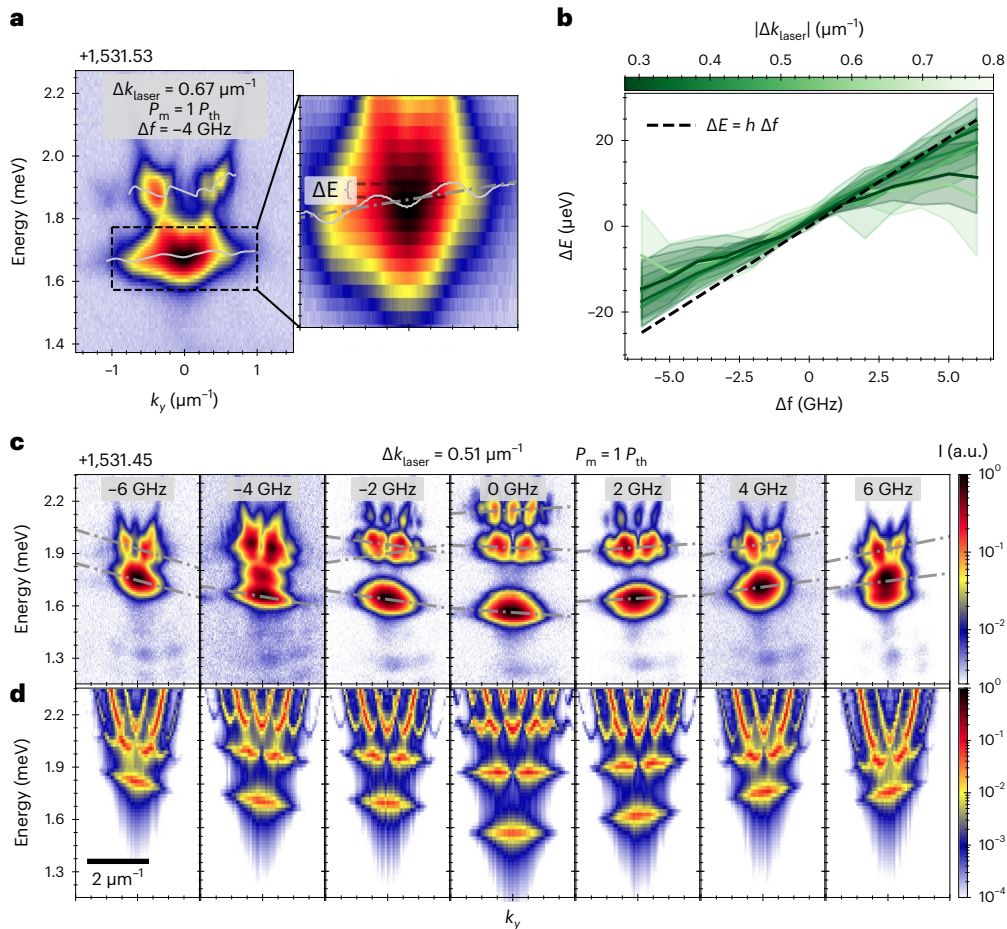


**Fig. 2 | Universal band tilting in a moving conveyor.** **a**, An example band structure of a moving conveyor. The thin light-grey line is the result of spectral peak finding and clustering. The dashed grey lines are linear fits to this clustered data. The energy shift at the BZ boundary  $\Delta E$  (inset) is extracted from the linear fit. **b**, The average (from 50–200 samples) energy shift at the BZ boundary as a function of the frequency for different modulation laser angles. Errors (shaded

regions) are estimated by averaging over datasets with different  $P_m$  and over different bands in each band structure. **c**, Experimental band structures for a fixed  $\Delta k_{\text{laser}}$  and  $P_m$  as a function of frequency between the pump lasers. **d**, The simulated far-field emission of Floquet–Bloch solutions to the fitted polariton Hamiltonian for the parameters in **c**.

the pump-generated carriers<sup>28</sup> are reduced to an effective potential  $V_{\text{eff}}$  for the exciton field  $\chi$ , expressed as

$$\begin{aligned} i\hbar\partial_t\psi &= -\frac{\hbar^2\nabla^2}{2m_{\text{eff}}}\psi + \hbar\Omega_R\chi - \frac{\delta}{2}\psi + V_{\text{shift}}\psi \\ i\hbar\partial_t\chi &= V_{\text{eff}}\cos(\Delta k_{\text{laser}}x - 2\pi\Delta f t)\chi + \hbar\Omega_R\psi + \frac{\delta}{2}\chi + V_{\text{shift}}\chi, \end{aligned} \quad (1)$$

where  $\psi$  is the photon field,  $m_{\text{eff}}$  is the photon effective mass,  $\delta$  is the exciton–photon detuning,  $V_{\text{shift}}$  is the average energy of excitons and photons and  $2\hbar\Omega_R$  is the photon–exciton Rabi splitting. The exciton mass can be safely neglected as it is much larger (by five orders of magnitude) than that of the photon. The Bloch bands of equation (1) were calculated numerically, and a least-squares fitting to the experimental splitting between  $s$  and  $p$  bands (Fig. 1c, thin light-grey lines) was used to estimate  $V_{\text{eff}}$ , after which the  $s$  band energy was used to estimate  $V_{\text{shift}}$ . The results of this fit are superimposed on Fig. 1c (dashed black), displaying good agreement in the band energies and momentum structures of the model and the dispersion spectra.

When  $|\Delta f| > 0$ , the laser interference pattern that creates the lattice potential moves along the surface of the microcavity. The direction of movement of this conveyor belt is controlled by the signs of  $\Delta f$  and  $\Delta k_{\text{laser}}$ . For positive (negative)  $\Delta f$ , the conveyor belt moves in the same (opposite) direction as  $\Delta k_{\text{laser}}$ . Bands are still present in the far-field

emission of the microcavity, but in response to the lattice motion they become tilted with respect to the momentum axis (Fig. 2a). These bands are non-reciprocal in that the energy of a Bloch wave will depend on its direction of motion, with higher-energy emission coming from waves moving in the same direction of motion as the conveyor belt, which can be intuitively understood as the Doppler effect. This non-reciprocity is quantified by measuring the tilt of the bands, extracted from the energy difference between the forward and backward edges of the BZ, that is,  $\Delta E = E(\pi/a) - E(-\pi/a)$  (Fig. 2a, inset), which is linearly proportional to  $\Delta f$ . The constant of proportionality is universal and independent of  $\Delta k_{\text{laser}}$  and  $P_m$  and corresponds to Planck’s constant (Fig. 2b).

This universality can be understood by considering the space–time Floquet–Brillouin zone where band tilting arises from topological winding around the  $1 + 1\text{D}$  unit cell<sup>6</sup>. It is known that the tilting energy in classical waves is connected to the Chern number  $C_n$  of the band  $\Delta E = C_n\hbar\Delta f$  (ref. 41), but the argument is generally applicable to any wave in a spatio-temporally periodic medium.

This can be proven by considering the quasi-energy of the Floquet state in terms of the instantaneous normalized eigenfunctions  $\psi_k(t)$  and energies  $\epsilon_k(t)$  (ref. 42). In the case of adiabatic evolution, it can be expressed as

$$\Omega_k = \frac{1}{T} \int_0^T dt \epsilon_k(t) + \frac{1}{T} \text{Im} \left[ \int_0^T dt \langle \psi_k | \partial_t \psi_k \rangle \right],$$

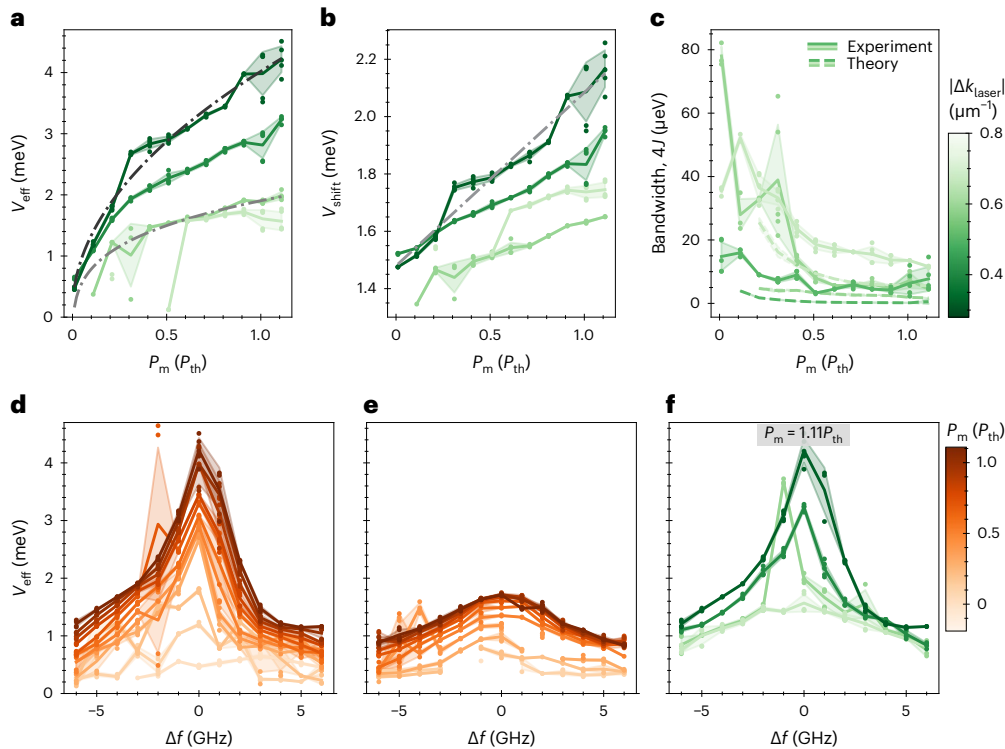


**Fig. 3 | Formation dynamics of a non-resonant potential.** **a**, The average fitted effective potential depth  $V_{\text{eff}}$  as a function of  $P_m$  for different  $\Delta k_{\text{laser}}$  values (colour key). Dash-dotted dark-grey and light-grey lines are the square root and fourth root fits for long and short period lattices, respectively. **b**, The average fitted potential shift  $V_{\text{shift}}$  as a function of  $P_m$  for different  $\Delta k_{\text{laser}}$ . The dash-dotted dark grey line is the linear fit to long-period lattices. **c**, The average

ground-state bandwidth as a function of  $P_m$  for the experiment (solid) and fitted theory (dashed). **d, e**, the average effective potential depth as a function of  $\Delta f$ , for varying  $P_m$  and  $\Delta k_{\text{laser}}$  values of  $0.32 \mu\text{m}^{-1}$  (**d**) and  $0.67 \mu\text{m}^{-1}$  (**e**). **f**, The average effective potential depth as a function of  $\Delta f$ , for fixed  $P_m$  and varying  $\Delta k_{\text{laser}}$ . Errors (shaded) and averages (solid lines) are estimated by averaging up to five different realizations with the same parameters.

where the first term is the dynamical phase acquired from eigenstate evolution and the second is the Berry phase acquired from the specific path taken in parameter space during the adiabatic evolution. The difference between the  $n$ th band quasi-energies at the two BZ edges can be written as the winding of the Berry phase around the Floquet–Brillouin zone thus

$$\Delta E_n = \hbar (\Omega_{\pi/L} - \Omega_{-\pi/L}) = \frac{\hbar}{T} \oint_{\text{BZ}} dk d\mathbf{k} \text{Im} \left[ \int_0^T dt \langle \psi_{\mathbf{k}} | \partial_t \psi_{\mathbf{k}} \rangle \right]$$

which is equal to the Chern number  $C_n$  of the band, so

$$\Delta E = \hbar |\Delta f| C_n.$$

Numerical calculation of the Chern numbers using the direct diagonalization eigenfunctions of equation (1) confirms that the Chern number of all bands is the same, that is,  $C_n = \pm 1 = \text{sign}(\Delta f)$ , and that topological edge modes are present under closed boundary conditions (Supplementary Section III). Additional agreement comes when comparing the experimental far-field patterns as a function of frequency (Fig. 2c) with the simulated far-field emission pattern of randomly occupied Floquet–Bloch bands (Fig. 2d). There is good agreement in the band splitting, anharmonicity and momentum structure in addition to the tilting magnitude and direction of the bands. For larger lattice periods (Fig. 1c, middle and Supplementary Section IV), the theory starts to deviate from experiment with regard to the anharmonicity of higher-order bands, with experimental bands being more closely separated than the theory predicts. An extension of equation (1) to include complex potentials<sup>27,43</sup> can improve the agreement between

theory and experiment (Supplementary Section IV), but nonetheless, the present theory accurately captures the observed band tilting for all parameters studied.

An additional feature in the frequency dependence of the bands is the reduction of the separation between them, indicating a reduction in the confining potential and setting a limit on the speed at which non-resonant optical potentials can be used to modulate polariton condensates. To understand the microscopic behaviour behind the potential formation and its dynamical time scales, we present the results of the fitting procedure of equation (1) as a function of modulation depth, lattice period and frequency of the conveyor belt. For a static conveyor belt, the power and period dependence of  $V_{\text{eff}}$  and  $V_{\text{shift}}$  are shown in Fig. 3a,b. For lattices with large period ( $|\Delta k_{\text{laser}}| < 0.5 \mu\text{m}^{-1}$ ),  $V_{\text{shift}}$  is linearly proportional to  $P_m$  (Fig. 3b, dash-dotted) while  $V_{\text{eff}}$  has a square root dependence on  $P_m$  (Fig. 3a, dark-grey dash-dotted). As the lattice period gets smaller, both  $V_{\text{shift}}$  and  $V_{\text{eff}}$  decrease and have a less pronounced dependence on pump power. At the smallest periods ( $|\Delta k_{\text{laser}}| > 0.5 \mu\text{m}^{-1}$ ),  $V_{\text{eff}}$  shifts from a square root to a fourth root dependence on  $P_m$  (Fig. 3a, light-grey dash-dotted).

The detailed power dependence described above sets limits on the underlying microscopic processes that create the optical potential. These have typically been considered to be a single phenomenological excitonic reservoir, proportional to the pump laser and with its density pinned by stimulated scattering into the condensate, which implies that the shape and depth of the potential are pinned at threshold<sup>28,30–32,34</sup>. This explanation can capture the two different functional dependencies of the effective potential depth only by considering the relaxation processes from the free-carrier plasma ( $n_{\text{eh}}$ ). At typical estimated experimental plasma densities ( $\sim 10^9 \text{ cm}^{-2}$ ; Supplementary Section V), excitons form through both geminate ( $\propto n_{\text{eh}}$ ) and bimolecular processes ( $\propto n_{\text{eh}}^2$ )

(ref. 44). Given that the plasma density is proportional to the laser intensity  $I_{\text{laser}} = P_1 + P_m + 2\sqrt{P_1 P_m} \cos(\Delta k_{\text{laser}} x)$ , it follows that the exciton reservoir density has both square and fourth root terms ( $n_R \propto n_{\text{eh}}^2 \propto \sqrt{P_m}, \sqrt[4]{P_m}$ , Supplementary Section V), which qualitatively and intuitively explain the observed potential's dependencies on increasing modulation power in Fig. 3. Additional processes such as exciton diffusion, the non-Hermitian potential<sup>27,43</sup> and direct interaction with the electron–hole plasma<sup>45</sup> need to be included to explain the simultaneous reduction in potential depth with the change in power dependence. However, despite the potential for additional refinement, there is order-of-magnitude agreement between the directly measured nearest-neighbour hopping  $J$  (Fig. 1c, green label and Fig. 3c, solid lines) and the hopping from of the fitted model (Fig. 3c, dashed lines). As expected for tightly bound sites, the hopping strength decreases approximately exponentially as a function of  $P_m$  and increases with smaller lattice period, while the measured hopping is of magnitude comparable to that inferred in previous experiments using optical confinement<sup>30,31,46</sup>.

The results of the least squares fitting for the potential depth as a function of  $\Delta f$  is shown in Fig. 3d,e (for fixed lattice periods) and Fig. 3f (for fixed modulation power). The datasets for other  $\Delta k_{\text{laser}}/P_m$  are qualitatively similar, and all share two main features: the potential depth decreases with increasing frequency offset, and it saturates at a non-zero value at high frequency. Firstly, the functional form of the decay changes with lattice period, with large period lattices (Fig. 3d) having a sharper decay curve as compared with short period lattices (Fig. 3e). Nonetheless, the decay constant ( $\tau_{\text{decay}} = 210 \pm 80$  ps) is independent of  $P_m$  and  $\Delta k_{\text{laser}}$  (Supplementary Section VI) and corresponds to the inability of the exciton reservoir to adiabatically follow the movement of the laser fringes. The similarity between the measured  $\tau_{\text{decay}}$  and previous measurements of relaxation time scales<sup>47</sup> supports the conclusion that the reduction in potential depth is due to the slow relaxation from the free-carrier plasma to the exciton reservoir. Secondly, the saturation value of  $V_{\text{eff}}$  at high  $\Delta f$  is independent of  $\Delta k_{\text{laser}}$  (Fig. 3f) and is 20–75% of the value at  $\Delta f = 0$  (see also Supplementary Section VI). The fact that this remaining potential lattice is independent of the lattice period suggests that it arises directly from interaction of the polaritons with the free carriers<sup>45</sup> before any relaxation processes and scatterings start to introduce spatial diffusion and scattering. Hence, both the decay and saturation of  $V_{\text{eff}}$  with increasing modulation speed can be explained within the same phenomenological framework: a free-carrier plasma that instantaneously follows the laser intensity and an exciton reservoir that is thermally populated from this plasma and feeds the condensate via stimulated scattering. This means that, while slow modulation ( $\Delta f < 1/210$  ps) will always be strongest, it is possible to use the electron–hole plasma to modulate the energy of GaAs polaritons faster than their thermal relaxation time scale. This is crucial to achieve effective Floquet Hamiltonians in the high-frequency approximation, which would allow the generation of artificial gauge fields<sup>48,49</sup>. Given a typical hopping measured in this work ( $J = 5$   $\mu\text{eV}$ ), the high-frequency regime is within experimental reach ( $\Delta f = 10$  GHz corresponds to 40  $\mu\text{eV}$  modulation).

## Discussion

We have demonstrated the formation of spatio-temporal potential lattices in exciton–polariton condensates. Using the simple interference between two lasers, we have created potential lattices with a controllable depth (up to ~4 meV) and tunable nearest-neighbour hopping. Detailed power and frequency dependencies of the potential depth have highlighted the crucial role of the electron–hole plasma in the formation of the non-resonant potential, demonstrating that modulation is possible at speeds higher than the thermal relaxation. Finally, we observed universal tilting of bands in the adiabatic modulation limit and directly linked it to non-trivial Chern numbers  $C_n = \pm 1$  of the instantaneous eigenstates, which is analogous to Thouless pumping in the limit

of a sliding lattice<sup>50–52</sup>. The non-zero Chern number demonstrates the topological non-triviality of the non-reciprocal tilting. The simplicity of the technique opens the door to future experiments using additional modulation frequencies<sup>53</sup> and extensions into two-dimensional geometries<sup>54</sup> that can result in higher Chern numbers<sup>41</sup> and lead to the experimental confirmation of topologically protected edge states in modulated polariton lattices. Additionally, the possibility of modulation at non-adiabatic speeds using the non-resonant plasma is a steppingstone towards creating artificial gauge fields and opens the door to studying Floquet topological phase transitions in polariton condensates<sup>35</sup> and other phase-coherent states in semiconductor microcavities<sup>55</sup> and studying the interplay between polariton non-Hermiticity, band topology and non-reciprocity.

## Online content

Any methods, additional references, Nature Portfolio reporting summaries, source data, extended data, supplementary information, acknowledgements, peer review information; details of author contributions and competing interests; and statements of data and code availability are available at <https://doi.org/10.1038/s41566-024-01424-z>.

## References

- Griffiths, D. J. & Schroeter, D. F. *Introduction to Quantum Mechanics* (Cambridge Univ. Press, 2018).
- Kitagawa, T., Berg, E., Rudner, M. & Demler, E. Topological characterization of periodically driven quantum systems. *Phys. Rev. B* **82**, 235114 (2010).
- Dutt, A. et al. A single photonic cavity with two independent physical synthetic dimensions. *Science* **367**, 59–64 (2020).
- Fang, K., Yu, Z. & Fan, S. Realizing effective magnetic field for photons by controlling the phase of dynamic modulation. *Nat. Photonics* **6**, 782–787 (2012).
- Ozawa, T. et al. Topological photonics. *Rev. Mod. Phys.* **91**, 015006 (2019).
- Thouless, D. J. Quantization of particle transport. *Phys. Rev. B* **27**, 6083–6087 (1983).
- Rudner, M. S. & Lindner, N. H. Band structure engineering and non-equilibrium dynamics in Floquet topological insulators. *Nat. Rev. Phys.* **2**, 229–244 (2020).
- Xu, S. & Wu, C. Space–time crystal and space–time group. *Phys. Rev. Lett.* **120**, 096401 (2018).
- Fleury, R., Sounas, D. L., Sieck, C. F., Haberman, M. R. & Alù, A. Sound isolation and giant linear nonreciprocity in a compact acoustic circulator. *Science* **343**, 516–519 (2014).
- Lira, H. Electrically driven nonreciprocity induced by interband photonic transition on a silicon chip. *Phys. Rev. Lett.* **109**, 033901 (2012).
- Sounas, D. L. & Alù, A. Non-reciprocal photonics based on time modulation. *Nat. Photonics* **11**, 774–783 (2017).
- Lindner, N. H., Refael, G. & Galitski, V. Floquet topological insulator in semiconductor quantum wells. *Nat. Phys.* **7**, 490–495 (2011).
- Nassar, H. et al. Nonreciprocity in acoustic and elastic materials. *Nat. Rev. Mater.* **5**, 667–685 (2020).
- Trainiti, G. & Ruzzene, M. Non-reciprocal elastic wave propagation in spatiotemporal periodic structures. *New J. Phys.* **18**, 083047 (2016).
- Adiyatullin, A. F. et al. Topological properties of floquet winding bands in a photonic lattice. *Phys. Rev. Lett.* **130**, 056901 (2023).
- Fedorova, Z., Qiu, H., Linden, S. & Kroha, J. Observation of topological transport quantization by dissipation in fast Thouless pumps. *Nat. Commun.* **11**, 3758 (2020).
- Weisbuch, C., Nishioka, M., Ishikawa, A. & Arakawa, Y. Observation of the coupled exciton–photon mode splitting in a semiconductor quantum microcavity. *Phys. Rev. Lett.* **69**, 3314–3317 (1992).

18. Byrnes, T., Kim, N. Y. & Yamamoto, Y. Exciton-polariton condensates. *Nat. Phys.* **10**, 803–813 (2014).
19. Schneider, C. et al. Exciton–polariton trapping and potential landscape engineering. *Rep. Prog. Phys.* **80**, 016503 (2017).
20. Jacqmin, T. et al. Direct observation of Dirac cones and a flatband in a honeycomb lattice for polaritons. *Phys. Rev. Lett.* **112**, 116402 (2014).
21. Jamadi, O. et al. Direct observation of photonic Landau levels and helical edge states in strained honeycomb lattices. *Light Sci. Appl.* **9**, 144 (2020).
22. Klemmt, S. et al. Exciton–polariton topological insulator. *Nature* **562**, 552–556 (2018).
23. Xu, X. et al. Interaction-induced double-sided skin effect in an exciton-polariton system. *Phys. Rev. B* **103**, 235306 (2021).
24. Mandal, S., Banerjee, R., Ostrovskaya, E. A. & Liew, T. C. H. Nonreciprocal transport of exciton polaritons in a non-Hermitian chain. *Phys. Rev. Lett.* **125**, 123902 (2020).
25. Xu, H. et al. Nonreciprocal exciton–polariton ring lattices. *Phys. Rev. B* **104**, 195301 (2021).
26. Sanvitto, D. et al. All-optical control of the quantum flow of a polariton condensate. *Nat. Photonics* **5**, 610–614 (2011).
27. Roumpos, G., Nitsche, W. H., Höfling, S., Forchel, A. & Yamamoto, Y. Gain-induced trapping of microcavity exciton polariton condensates. *Phys. Rev. Lett.* **104**, 126403 (2010).
28. Askitopoulos, A. et al. Polariton condensation in an optically induced two-dimensional potential. *Phys. Rev. B* **88**, 041308 (2013).
29. Cristofolini, P. et al. Optical superfluid phase transitions and trapping of polariton condensates. *Phys. Rev. Lett.* **110**, 186403 (2013).
30. Cherotchenko, E. D., Sigurdsson, H., Askitopoulos, A. & Nalitov, A. V. Optically controlled polariton condensate molecules. *Phys. Rev. B* **103**, 115309 (2021).
31. Ohadi, H. et al. Tunable magnetic alignment between trapped exciton-polariton condensates. *Phys. Rev. Lett.* **116**, 106403 (2016).
32. Alyatkin, S., Töpfer, J. D., Askitopoulos, A., Sigurdsson, H. & Lagoudakis, P. G. Optical control of couplings in polariton condensate lattices. *Phys. Rev. Lett.* **124**, 207402 (2020).
33. Pickup, L., Sigurdsson, H., Ruostekoski, J. & Lagoudakis, P. G. Synthetic band-structure engineering in polariton crystals with non-Hermitian topological phases. *Nat. Commun.* **11**, 4431 (2020).
34. Ohadi, H. et al. Synchronization crossover of polariton condensates in weakly disordered lattices. *Phys. Rev. B* **97**, 195109 (2018).
35. Ge, R., Broer, W. & Liew, T. C. H. Floquet topological polaritons in semiconductor microcavities. *Phys. Rev. B* **97**, 195305 (2018).
36. Gnusov, I. et al. Quantum vortex formation in the ‘rotating bucket’ experiment with polariton condensates. *Sci. Adv.* **9**, eadd1299 (2023).
37. del Valle-Inclan Redondo, Y. et al. Optically driven rotation of exciton–polariton condensates. *Nano Lett.* **23**, 4564–4571 (2023).
38. Kavokin, A. et al. Polariton condensates for classical and quantum computing. *Nat. Rev. Phys.* **4**, 435–451 (2022).
39. Wei, M. et al. Optically trapped room temperature polariton condensate in an organic semiconductor. *Nat. Commun.* **13**, 7191 (2022).
40. Luo, S. et al. Classical spin chains mimicked by room-temperature polariton condensates. *Phys. Rev. Appl.* **13**, 044052 (2020).
41. Nassar, H., Chen, H., Norris, A. N. & Huang, G. L. Quantization of band tilting in modulated phononic crystals. *Phys. Rev. B* **97**, 014305 (2018).
42. Berry, M. V. Quantal phase factors accompanying adiabatic changes. *Proc. R. Soc. Lond. Math. Phys. Sci.* **392**, 45–57 (1997).
43. Cristofolini, P., Hatzopoulos, Z., Savvidis, P. G. & Baumberg, J. J. Generation of quantized polaritons below the condensation threshold. *Phys. Rev. Lett.* **121**, 067401 (2018).
44. Piermarocchi, C., Tassone, F., Savona, V., Quattropani, A. & Schwendimann, P. Exciton formation rates in GaAs/Al<sub>x</sub>Ga<sub>1-x</sub>As quantum wells. *Phys. Rev. B* **55**, 1333–1336 (1997).
45. Pieczarka, M. et al. Crossover from exciton–polariton condensation to photon lasing in an optical trap. *Opt. Express* **30**, 17070–17079 (2022).
46. Pieczarka, M. et al. Topological phase transition in an all-optical exciton–polariton lattice. *Optica* **8**, 1084–1091 (2021).
47. Damen, T. C. et al. Dynamics of exciton formation and relaxation in GaAs quantum wells. *Phys. Rev. B* **42**, 7434–7438 (1990).
48. Goldman, N. & Dalibard, J. Periodically driven quantum systems: effective Hamiltonians and engineered gauge fields. *Phys. Rev. X* **4**, 031027 (2014).
49. Aidelsburger, M., Nascimbene, S. & Goldman, N. Artificial gauge fields in materials and engineered systems. *C. R. Phys.* **19**, 394–432 (2018).
50. Wang, L., Troyer, M. & Dai, X. Topological charge pumping in a one-dimensional optical lattice. *Phys. Rev. Lett.* **111**, 026802 (2013).
51. Lohse, M., Schweizer, C., Zilberberg, O., Aidelsburger, M. & Bloch, I. A Thouless quantum pump with ultracold bosonic atoms in an optical superlattice. *Nat. Phys.* **12**, 350–354 (2016).
52. Nakajima, S. et al. Topological Thouless pumping of ultracold fermions. *Nat. Phys.* **12**, 296–300 (2016).
53. Fu, Q., Wang, P., Kartashov, Y. V., Konotop, V. V. & Ye, F. Nonlinear Thouless pumping: solitons and transport breakdown. *Phys. Rev. Lett.* **128**, 154101 (2022).
54. Rechtsman, M. C. et al. Photonic Floquet topological insulators. *Nature* **496**, 196–200 (2013).
55. Hu, J. et al. Polariton laser in the Bardeen–Cooper–Schrieffer regime. *Phys. Rev. X* **11**, 011018 (2021).

**Publisher’s note** Springer Nature remains neutral with regard to jurisdictional claims in published maps and institutional affiliations.

**Open Access** This article is licensed under a Creative Commons Attribution 4.0 International License, which permits use, sharing, adaptation, distribution and reproduction in any medium or format, as long as you give appropriate credit to the original author(s) and the source, provide a link to the Creative Commons licence, and indicate if changes were made. The images or other third party material in this article are included in the article’s Creative Commons licence, unless indicated otherwise in a credit line to the material. If material is not included in the article’s Creative Commons licence and your intended use is not permitted by statutory regulation or exceeds the permitted use, you will need to obtain permission directly from the copyright holder. To view a copy of this licence, visit <http://creativecommons.org/licenses/by/4.0/>.

© The Author(s) 2024

## Methods

### Sample

The microcavity sample used consisted of 35 (30) AlAs/Al<sub>0.15</sub>Ga<sub>0.85</sub>As mirror pairs for the bottom (top) distributed Bragg reflectors (DBRs) forming a  $5\lambda/2$  cavity ( $\lambda$  being the resonance wavelength) with four sets of  $(3 \times 13)$ -nm-wide GaAs/Al<sub>0.3</sub>Ga<sub>0.7</sub>As. As quantum wells, leading to a Rabi splitting of  $2\hbar\Omega \approx 8.5$  meV. At  $k \approx 0$ , the cavity energy was 7 meV below the exciton energy and the lower polariton lifetime was 22 ps.

### Laser interference

Two continuous wave lasers were used to simultaneously excite the microcavity: a single-mode, cavity-locked Ti:sapphire ( $\sim 120$  mW =  $1.2P_{\text{th}}$ ) and a single-mode, tapered amplifier (TA) semiconductor laser ( $< 1$  W, 20 GHz mode-hop free tuning, 1–90% of Ti:sapphire power). Both lasers were chopped into  $\sim 10$   $\mu$ s pulses synchronized with the camera capture using acousto-optic modulators to prevent sample heating and defocused with a cylindrical lens, providing a  $50 \times 16$   $\mu$ m elliptical condensate on the microcavity.

The TA was offset from the Ti:sapphire both in angle and in frequency, creating intensity fringes on the sample surface ( $a = 9$ – $20$   $\mu$ m) that moved with speeds of up to  $0.2$   $\mu$ m ps<sup>-1</sup>. To achieve the angle offset, both lasers were initially aligned at normal incidence on the microcavity, and the TA was beam-walked to come in at a variable angle ( $0.3$ – $0.7$   $\mu$ m<sup>-1</sup>) while maintaining maximal spatial overlap. The frequency offset was controlled via the output grating of the laser diode of the TA and monitored using the beat signal between the two lasers measured on a fast photodiode. The modulation range was 20 GHz with an accuracy of 100 MHz (mostly limited by slow frequency drift).

### Measurement

The sample was held in a continuous-flow helium cryostat at 4 K. An objective with a numerical aperture of 0.4 was used to focus the lasers and collect the emitted photoluminescence, which was separated from the laser light using a dichroic mirror. The photoluminescence passed through a high-resolution spectrometer (with a minimum full-width at half-maximum of  $\sim 60$   $\mu$ eV) and was then imaged with a charge-coupled device camera.

### Band analysis

To extract the experimental band structures, images were smoothed, and energy peaks were detected for each value of momentum  $k_y$  and then clustered using the AgglomerativeClustering function in scikit-learn<sup>56</sup>. The clustering metric prioritizes clustering along the mode momenta and takes into consideration the energy tilting for non-zero frequency offset between the lasers. Peak fitting and clustering were supervised to ensure consistent results for all experimental conditions.

### Data availability

Raw data is available on figshare at <https://doi.org/10.6084/m9.figshare.25217435> (ref. 57).

## Code availability

The code used to analyse data and perform simulations are both available via GitHub at <https://github.com/YagoDel/microcavities> (ref. 58).

## References

56. Pedregosa, F. et al. Scikit-learn: machine learning in Python. *J. Mach. Learn. Res.* **12**, 2825–2830 (2011).
57. del Valle Inclan Redondo, Y. et al. Non-reciprocal band structures in an exciton–polariton Floquet optical lattice. *figshare* <https://doi.org/10.6084/m9.figshare.25217435> (2024).
58. del Valle Inclan Redondo, Y. Microcavities. *GitHub* <https://github.com/YagoDel/microcavities> (2023).

## Acknowledgements

The authors acknowledge financial support by the Japan Society for the Promotion of Science Grants-in-Aid for Scientific Research (KAKENHI; grant nos. JP17H04851 and JP19H0561), Japan Science and Technology Agency PRESTO grant no. JPMJPR1768, NTT Research and the State of Bavaria. T.C.H.L. was supported by the Singapore Ministry of Education via the AcRF Tier 3 Program ‘Geometrical Quantum Materials’ (MOE2018-T3-1-002). X.X. was supported by the National Natural Science Foundation of China (grant no. 12264061). E.A.O. was supported by the Australian Research Council Centre of Excellence Grant CE170100039. The Würzburg group acknowledges financial support by the German Research Foundation under Germany’s Excellence Strategy – EXC2147 ‘ct.qmat’ (project id 390858490).

## Author contributions

Y.d.V.I.R. and M.D.F. conceived, designed and performed the experiments. Y.d.V.I.R. collected and analysed the experimental data. X.X. and T.C.H.L. conceived the numerical model. Y.d.V.I.R. and X.X. performed the computations. E.A.O., T.C.H.L., A.S. and R.T. provided the theoretical and analytical framework. C.S., S.D., S.K. and S.H. designed, fabricated and characterized the sample. S.T. and M.D.F. supervised the project. The paper was prepared by Y.d.V.I.R. and M.D.F., with review and editing carried out by all authors.

## Competing interests

The authors declare no competing interests.

## Additional information

**Supplementary information** The online version contains supplementary material available at <https://doi.org/10.1038/s41566-024-01424-z>.

**Correspondence and requests for materials** should be addressed to Yago del Valle Inclan Redondo or Michael D. Fraser.

**Peer review information** *Nature Photonics* thanks the anonymous reviewers for their contribution to the peer review of this work.

**Reprints and permissions information** is available at [www.nature.com/reprints](http://www.nature.com/reprints).